Article

Not peer-reviewed version

Preparation of V_2O_5 Composite Cathode Material Based on In-Situ Intercalated Polyaniline and Its High-Performance Aqueous Zinc-Ion Battery Applications

Shilin Li , Taoyun Zhou * , Yun Cheng , Xinyu Li

Posted Date: 30 March 2025

doi: 10.20944/preprints202503.2231.v1

Keywords: aqueous zinc-ion batteries (AZIBs); in-situ intercalation; polyaniline modification; electrochemical performance

Article

Preparation of V_2O_5 Composite Cathode Material Based on In-Situ Intercalated Polyaniline and Its High-Performance Aqueous Zinc-Ion Battery Applications

Shilin Li [1], Taoyun Zhou [1,*], Yun Cheng [1] and Xinyu Li [2]

[1] School of Information, Hunan University of Humanities, Science and Technology, Loudi 417000, China; lishilin09@huhst.edu.cn (S.L.); yuncheng@huhst.edu.cn (Y.C.)

[2] College of Physics and Electronic Information Engineering & Key Laboratory of Low-dimensional Structural Physics and Application, Education Department of GuangxiZhuang Autonomous Region, Guilin University of Technology, Guilin 541004, China; lixinyu5260@163.com (X.L.)

* Correspondence: taoyun_2000@163.com

Abstract: With the rapid development of renewable energy, efficient and stable energy storage technologies have become a research focus in the energy sector. Aqueous zinc-ion batteries (AZIBs) hold great promise for electrochemical energy storage due to their high safety, abundant zinc resources, high theoretical specific capacity, and low redox potential. However, AZIBs still face challenges such as low electronic conductivity, sluggish ion migration kinetics, zinc dendrite growth, and side reactions, which severely limit their practical applications. To address the issues of the large zinc-ion radius and the restricted interlayer spacing of vanadium oxides, this study proposes an innovative in-situ intercalation polyaniline (PANI) molecular modification strategy. A flower-like organic-inorganic hybrid material, PANI-V_2O_5 , is successfully synthesized via a synchronous oxidative polymerization method. This strategy effectively regulates the interlayer spacing of vanadium oxides without introducing inert cations, significantly enhancing the material's conductivity and structural stability while accelerating zinc-ion diffusion kinetics. Electrochemical tests demonstrate that PANI-V_2O_5 exhibits a high specific capacity of up to 450 $mAh \cdot g^{-1}$ at a current density of 0.1 $A \cdot g^{-1}$ and retains 96.7% of its capacity after 300 cycles at 1 $A \cdot g^{-1}$, showcasing excellent cycling stability and rate performance. This study provides new insights into the design of high-performance cathode materials for zinc-ion batteries and lays a theoretical and experimental foundation for the development of efficient and stable energy storage systems in the future.

Keywords: aqueous zinc-ion batteries (AZIBs); in-situ intercalation; polyaniline modification; electrochemical performance

---

1. Introduction

In recent years, coal-based energy has caused significant environmental issues, posing severe challenges to the principle of sustainable development in modern society [1–3]. Against this backdrop, renewable energy sources, represented by electricity, have gradually emerged as a crucial part of the energy system [4–6]. Among them, clean energy sources such as wind and solar power play a key role in energy conversion due to their broad application prospects. However, the efficient utilization of renewable energy relies on advancements in energy storage technologies, with secondary batteries - particularly lithium-ion batteries (LIBs) - playing an indispensable role in energy storage systems [7,8].

Despite dominating the energy storage field, lithium-ion batteries still face several challenges. The primary concern is the scarcity of lithium resources, as lithium reserves are limited and unevenly distributed. The rising cost of lithium in the future may further hinder its widespread application. Moreover, the organic electrolytes used in lithium-ion batteries pose safety risks, including flammability and explosion hazards during charge-discharge cycles, which create additional challenges for large-scale deployment [9–11]. Therefore, the development of alternative secondary battery systems that are resource-abundant and safer has become a crucial research direction to replace lithium-ion batteries.

In recent years, sodium-ion batteries (SIBs) and potassium-ion batteries (PIBs) have attracted widespread attention due to their abundant raw material reserves and low cost [12]. However, the high chemical reactivity of Na^+ and K^+ poses significant safety risks, and their relatively large ionic radii makes it challenging to find suitable cathode and anode materials, further complicating their reversible storage [13].

Meanwhile, rechargeable batteries based on multivalent metal ions (such as Mg^{2+}, Ca^{2+}, Zn^{2+}, and Al^{3+} batteries) have become a research hotspot due to their high safety, high volumetric energy density, and abundant crustal reserves. However, one of the key challenges these batteries face is the development of a reversible electrolyte system compatible with magnesium, calcium, or aluminum metal anodes. Existing electrolytes often corrode metal anodes or current collectors, leading to the formation of inactive surface layers, which hinder the reversible charge-discharge process of the battery [14–16].

Among various alternative energy storage systems, zinc-ion batteries (ZIBs) have rapidly gained widespread attention due to their unique advantages [17–19]. As an anode material, zinc offers several significant benefits: (1) It is compatible with both aqueous and non-aqueous electrolytes, enhancing system safety. (2) Zinc has a relatively high redox potential (-0.763 V vs. the standard hydrogen electrode), allowing ZIBs to operate stably in aqueous electrolytes—a challenge for many other mobile-ion batteries [20,21]. (3) Compared to lithium-ion batteries (LIBs), ZIBs offer higher safety and lower environmental risks. (4) The reversible plating/stripping characteristics of zinc enable ZIBs to function in near-neutral or mildly acidic electrolytes (pH = 3.6-6.0), effectively suppressing zinc dendrite formation and the side-product ZnO, thereby ensuring a long cycle life. (5) ZIBs exhibit a volumetric energy density of up to 5855 mAh cm^{-3}, significantly higher than LIBs (2061 mAh cm^{-3}), owing to the high density of Zn and its two-electron redox reaction mechanism. As a result, ZIBs hold great potential for applications in miniaturized devices, such as wearable sensors and implantable medical devices, demonstrating promising commercialization prospects [22].

Although aqueous zinc-ion batteries (ZIBs) offer numerous advantages, research on their key electrode material - vanadium-based oxides - is still in the exploratory stage. Given the high safety, low cost, and environmental friendliness of AZIBs, modifying vanadium-based oxides holds significant scientific importance [23,24]. However, these materials still suffer from several drawbacks, including sluggish kinetics, poor electronic conductivity, structural collapse during cycling, and vanadium dissolution [25,26].

Compared to lithium-ion batteries, zinc ions experience stronger electrostatic interactions during intercalation, which restricts ion diffusion and accelerates capacity decay [26,27]. To address this issue, pre-intercalation techniques have been proposed to facilitate Zn^{2+} diffusion between the layers of vanadium-based materials and effectively regulate the crystal structure of electrode materials [28–30]. Additionally, pre-intercalated materials serve as structural supports, maintaining electrode stability after Zn^{2+} extraction and thereby enhancing cycle life. Common pre-intercalation strategies include ion pre-intercalation and molecular pre-intercalation [30]. While ion pre-intercalation can improve structural stability to some extent, molecular pre-intercalation - especially with conductive polymers - has proven to be more effective. Due to their larger molecular size, conductive polymers can significantly expand the interlayer spacing of vanadium oxides, promoting Zn^{2+} diffusion within the crystal structure [23,31–35]. Furthermore, the insolubility of conductive polymers in electrolytes helps maintain the stability of the intercalated structure during cycling.

Preprints.org (www.preprints.org) | NOT PEER-REVIEWED | Posted: 30 March 2025 doi:10.20944/preprints202503.2231.v1

Among various vanadium-based oxide materials, V_2O_5 has been widely used as a cathode material for AZIBs due to its variable valence states (+2 to +5), multi-electron redox reactions, abundant crustal reserves, and tunable crystal structure [36,37]. V_2O_5 possesses a typical layered structure, where VO_5 square pyramids are linked into sheets, with weak vanadium-oxygen bonds connecting adjacent layers. This unique layered structure provides ideal diffusion channels for Zn^{2+}intercalation/deintercalation, enabling a theoretical capacity of 589 mAh·g^{-1}. However, due to the high charge density and relatively large radius of Zn^{2+}, the Zn^{2+} storage performance of V_2O_5 still faces challenges such as slow insertion kinetics and poor cycling stability [38].

To enhance the zinc storage performance of V_2O_5, researchers have explored various strategies, including metal cation doping, structural water pre-intercalation, and organic group modifications, to improve the stability and electrochemical reversibility of its layered structure. Chou and his team successfully synthesized V_2O_5-x/PANI superlattice composites using a hydrothermal reaction method by introducing polyaniline (PANI) into the interlayers of V_2O_5 [39]. Their study found that the PANI layers not only prevented the dissolution of V_2O_5-x in aqueous solutions but also expanded the interlayer spacing and weakened the electrostatic interaction between Zn^{2+} and O^{2-}, thereby enhancing the reversible Zn^{2+} storage performance. Similarly, Kumankuma et al. developed a PEDOT@YVO composite material, where the incorporation of the conductive polymer PEDOT effectively increased the interlayer spacing of YVO, achieving a high initial specific capacity of 308.5 mAh·g^{-1} at a 0.2 C rate [40].

In this study, without introducing inactive cations, it proposes an innovative molecular modification strategy based on synchronous oxidative polymerization. By precisely controlling the self-assembly process of vanadate and aniline precursors, it successfully constructs an organic-inorganic hybrid composite material (PANI-V_2O_5) with tunable interlayer spacing. This strategy not only effectively expands the interlayer spacing of V_2O_5, improving its electronic and ionic conductivity, but also enhances its structural stability, thereby significantly improving the zinc-ion diffusion kinetics within the electrode material. Systematic electrochemical tests validate the superior performance of the PANI-V_2O_5 composite material in aqueous zinc-ion batteries (AZIBs). The results demonstrate that this novel PANI-V_2O_5 hybrid material not only provides a new design approach for high-performance aqueous ZIB cathode materials but also lays a solid foundation for enhancing the practical applications of zinc-ion batteries.

2. Materials and Methods

2.1. Materials

In this study, a simple hydrothermal method is employed to synthesize polyaniline-intercalated vanadium oxide (PANI-V_2O_5) organic-inorganic composite material. The specific steps are as follows. Firstly, 1.5 g of NH_4VO_3 crystals are weighed and placed in a beaker, followed by the addition of 60 mL of deionized water. The mixture is subjected to ultrasonic treatment for 30 minutes to ensure complete dissolution of NH_4VO_3, forming a light yellow solution. Subsequently, the beaker is placed in a 0°C environment, and a certain amount of aniline solution is slowly added dropwise while stirring. Simultaneously, 2.2 mol·L^{-1} dilute hydrochloric acid is used to adjust the pH of the solution to approximately 3.

After stirring for 5 hours, the obtained solution is transferred into a Teflon-lined autoclave and subjected to a hydrothermal reaction at 140°C for 24 hours. Upon completion of the reaction, the product is collected and repeatedly washed with deionized water and ethanol to remove any unreacted impurities. Finally, the sample is dried in an oven at 60°C for 12 hours, yielding the PANI-V_2O_5 composite material.

2.2. Characterization of Cathode Material

2.2.1. Scanning Electron Microscopy (SEM) and Energy Dispersive Spectroscopy (EDS)

The SEM and EDS test results are shown in Figure 1, which characterizes the microstructure and elemental composition of V_2O_5 and PANI - V_2O_5 composite materials.

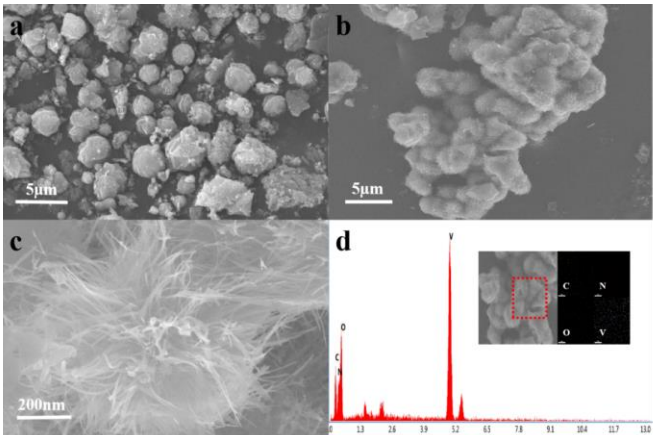

Figure 1. (**a**) SEM image of pure V_2O_5; (**b**,**c**) SEM images of PANI-V_2O_5, showing its microstructural changes; (**d**) EDS image of PANI-V_2O_5, illustrating the elemental composition and distribution.

Figure 1a presents the SEM image of V_2O_5 obtained without the addition of aniline monomers. It can be observed that V_2O_5 exhibits irregular spherical particles with a rough surface. The particle size distribution is uniform, and the particles are densely packed together. This compact structure may impose certain limitations on the ion transport capability of the material.

Figure 1b illustrates the morphology of V_2O_5 after the introduction of PANI. Compared to pure V_2O_5, the morphology of PANI-V_2O_5 undergoes significant changes, with the surface becoming more porous and less compact. Additionally, spiky, sea-urchin-like structures measuring approximately 2 - 5 nm can be observed on the surface of PANI-V_2O_5. These morphological changes indicate that PANI doping induces a rearrangement of the V_2O_5 internal structure, optimizing the particle aggregation state. This structural adjustment not only increases the specific surface area of the material but also enhances the permeability of electrolyte ions, thereby improving its electrochemical performance.

Figure 1c further presents an enlarged view of the nanostructure of PANI-V_2O_5. Clearly visible are nanofiber-like structures on the material surface, with fiber diameters in the tens of nanometers range. These nanofibers originate from the growth of PANI, confirming the successful doping of PANI. The nanofiber structure significantly increases the material’s specific surface area, providing more active sites, while also effectively shortening the diffusion pathways for electrolyte ions, thereby enhancing the kinetics of the electrochemical reactions.

Figure 1d shows the EDS test results, which analyze the elemental composition and distribution of the material. The test results reveal the uniform presence of vanadium (V), oxygen (O), carbon (C), and nitrogen (N) in the sample, with C and N originating from PANI molecules. This further confirms the successful intercalation of PANI into the layered structure of V_2O_5. Additionally, the inset illustrates the spatial distribution of the elements, showing a homogeneous dispersion of all elements. This suggests that the introduction of PANI does not cause phase separation, ensuring the structural stability of the composite material. Such uniform elemental distribution plays a crucial role in enhancing the electrochemical stability of the material.

2.2.2. Transmission Electron Microscopy (TEM) Analysis

To further investigate the microstructure and morphological characteristics of PANI-V_2O_5, transmission electron microscopy (TEM) analysis is conducted. Figure 2 presents high-resolution TEM images of the PANI-V_2O_5 material, where Figure 2a shows the TEM image of V_2O_5 without polyaniline (PANI) incorporation, and Figure 2b displays the TEM image of PANI-V_2O_5 after PANI introduction.

 doi:10.20944/preprints202503.2231.v1

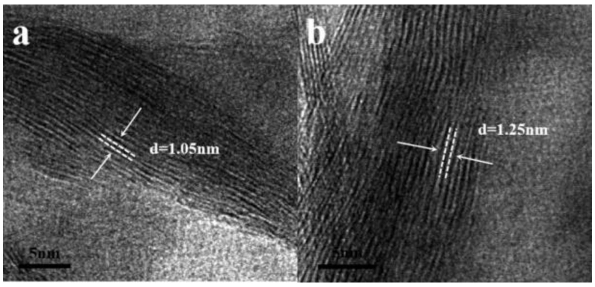

Figure 2. (**a**) TEM image of V_2O_5 without PANI doping; (**b**) TEM image of PANI-V_2O_5 after PANI doping.

As observed in Figure 2a, the pristine V_2O_5 exhibits a tightly stacked layered structure with an interlayer spacing of 1.05 nm, indicating a well-ordered lamellar arrangement. In contrast, Figure 2b shows that the interlayer spacing of PANI-V_2O_5 increases to 1.25 nm, exhibiting a relatively loosened layered structure. This change suggests that the successful intercalation of PANI expands the V_2O_5 interlayer spacing, primarily due to the introduction of PANI molecules, which increase electrostatic repulsion between layers and promote interlayer expansion.

The enlargement of interlayer spacing significantly impacts the electrochemical performance of the material. A larger interlayer spacing facilitates the penetration of electrolyte ions into the material, thereby reducing charge transfer resistance and enhancing ion diffusion rates, ultimately improving electrochemical energy storage performance. Therefore, PANI intercalation not only modifies the microstructure of V_2O_5 but also potentially enhances its energy storage capability, making it a promising candidate for energy storage devices and electrode materials.

2.2.3. X-Ray Diffraction (XRD) and Raman Spectroscopy Analysis

The results of X-ray diffraction (XRD) and Raman spectroscopy are shown in Figure 3, where Figure 3a presents the XRD patterns of V_2O_5 and PANI-V_2O_5, while Figure 3b shows the Raman spectra of both materials.

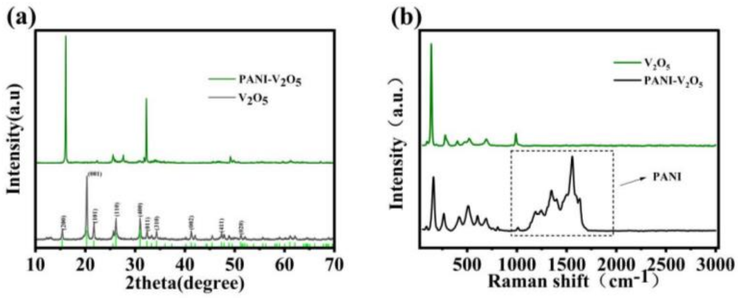

Figure 3. Characterization of pure V_2O_5 and PANI-V_2O_5 composite materials: (**a**) X-ray diffraction (XRD) patterns; (**b**) Raman spectroscopy comparative analysis.

In Figure 3a, the pure V_2O_5 sample (black curve) exhibits characteristic diffraction peaks of layered V_2O_5, with clearly visible reflections from the (001), (200), and (300) crystal planes. In contrast, the XRD pattern of the PANI-V_2O_5 composite (green curve) retains the main diffraction peaks of V_2O_5, indicating that the material maintains its layered structure. However, a noticeable shift of the (001) diffraction peak toward a smaller angle in the PANI-V_2O_5 spectrum suggests an increase in interlayer spacing due to PANI incorporation. This observation is consistent with the transmission electron microscopy (TEM) results, further confirming the successful intercalation of PANI.

To further evaluate the molecular structure and interactions of PANI-V_2O_5, Raman spectroscopy is performed in the range of 0-3000 cm^{-1}, with the results shown in Figure 3b. The Raman spectrum of pure V_2O_5 (green curve) exhibits characteristic V–O vibrational peaks. Meanwhile, the PANI - V_2O_5

 doi:10.20944/preprints202503.2231.v1

spectrum (black curve) retains the main Raman peaks of V_2O_5 while introducing new characteristic peaks at 1366, 1453, 1532, and 1562 cm^{-1}. These new peaks correspond to C–C stretching vibrations and symmetric/asymmetric C=C vibrations from the PANI molecules. Additionally, the inset in Figure 3b highlights the distinct PANI characteristic peaks, further confirming its successful intercalation into the layered V_2O_5 structure and the possible formation of an ordered supramolecular structure within the composite.

2.2.4. AnalysisX-Ray Photoelectron Spectroscopy (XPS) Analysis

Figure 4 presents the XPS analysis results of the PANI-V_2O_5 composite material, including the full spectrum and high-resolution spectra of individual elements.

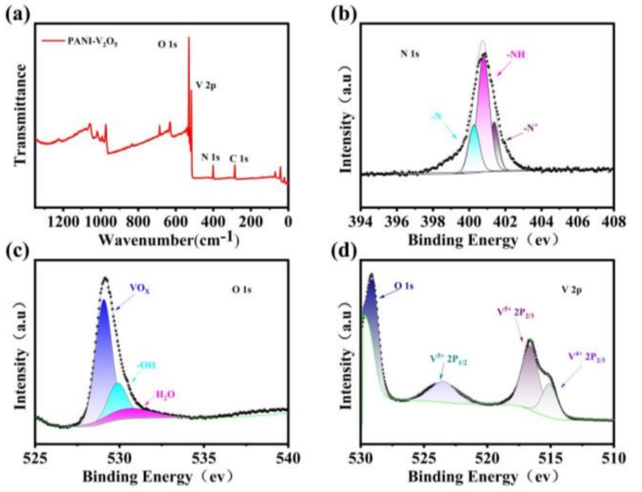

Figure 4. XPS analysis results. (**a**) Full XPS spectrum of the PANI-V_2O_5 sample; (**b**) High-resolution N 1s spectrum of PANI-V_2O_5; (**c**) High-resolution O 1s spectrum of PANI-V_2O_5; (**d**) High-resolution V 2p spectrum of PANI-V_2O_5.

Figure 4a shows the XPS spectrum of PANI-V_2O_5, clearly identifying characteristic peaks corresponding to C 1s, N 1s, O 1s, and V 2p, confirming the successful incorporation of PANI while maintaining the main structure of V_2O_5. The strong O 1s and V 2p peaks indicate that V_2O_5 remains the dominant component, whereas the presence of the N 1s peak further verifies the introduction of PANI.

Figure 4b displays the high-resolution N 1s spectrum, which can be deconvoluted into three distinct peaks: ~399 eV (N^-, originating from the aniline group in PANI), 400 eV (-NH-, corresponding to the imine structure in the PANI chain), and 401 eV (N^+, associated with the doped form of PANI, such as protonated structures). These peaks correspond to quinonoid rings (400.38 eV), benzenoid rings (400.73 eV), and quaternary ammonium (401.23 eV), respectively, indicating the presence of PANI in various oxidation states within the composite material. This diversity in oxidation states may enhance electron transport capability, thereby improving its electrochemical performance.

Figure 4c presents the XPS spectrum of O 1s, where three main peaks are observed: ~530.3 eV (VO_x, representing oxygen in V_2O_5), confirming that the material retains its layered V_2O_5 structure; 531.8 eV (-OH), suggesting the presence of hydroxyl groups, possibly due to PANI incorporation or water adsorption; and 533.5 eV (H_2O), likely attributed to adsorbed water within the material. These different oxygen environments indicate that PANI doping modulates the electronic structure of V_2O_5 to some extent, influencing its physicochemical properties.

Figure 4d presents the high-resolution V 2p spectrum, revealing the coexistence of $V^{4+}$and V^{5+}oxidation states. The peaks at 516.08 eV and 523.78 eV correspond to V^{4+}, suggesting partial reduction of V_2O_5 to VO_2, while the peaks at 517.28 eV and 524.98 eV are attributed to V^{5+}, which is primarily derived from the main V_2O_5 structure. The coexistence of $V^{4+}$and V^{5+}indicates favorable

 doi:10.20944/preprints202503.2231.v1

charge transfer characteristics, contributing to improved conductivity and electrochemical stability, thereby enhancing its potential for energy storage applications.

2.2.5. Nitrogen Adsorption-Desorption Analysis

To further investigate the pore size and porosity characteristics of the synthesized materials, nitrogen adsorption-desorption tests are conducted on both PANI-V_2O_5 and V_2O_5 samples. The results are shown in Figure 5.

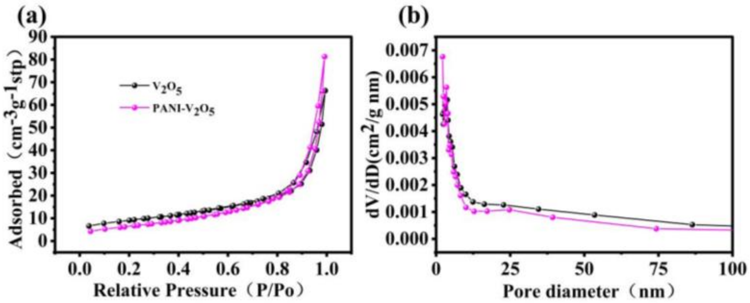

Figure 5. (**a**) Nitrogen adsorption-desorption isotherms of PANI-V_2O_5 and V_2O_5; (**b**) Corresponding pore size distribution curves.

Figure 5a presents the nitrogen adsorption-desorption isotherms of V_2O_5 and PANI-V_2O_5, both exhibiting typical Langmuir IV-type isotherm characteristics, indicating the presence of a significant mesoporous structure. In the low relative pressure range (P/P_0< 0.2), the adsorption volume remains low, suggesting minimal micropore contribution and predominantly mesoporous characteristics. As the relative pressure increases (P/P_0> 0.8), the specific surface area of PANI-V_2O_5 increases significantly from 66.13 m^2/g (for V_2O_5) to 81.28 m^2/g. This enhancement indicates that the introduction of PANI effectively increases porosity, enlarges the specific surface area, provides more exposed active sites, enhances electrolyte wettability, and facilitates Zn^{2+}storage capacity.

Figure 5b illustrates the pore size distribution of both materials, showing a predominant distribution below 25 nm, further confirming their mesoporous nature. Compared to V_2O_5, PANI-V_2O_5 exhibits a broader pore size distribution, with major peaks at approximately 2.21 nm and 17.19 nm. This suggests that PANI doping not only increases pore volume but also optimizes the pore structure. Such a hierarchical pore structure benefits rapid Zn^{2+}storage and release while improving electrolyte penetration and electron transport capability, thereby enhancing the electrochemical performance and cycling stability of the material.

3. Results and Analysis

3.1. Cyclic Voltammetry Tests

Figure 6 presents the cyclic voltammetry (CV) curves of PANI-V_2O_5 at a scan rate of 0.1 $mV \cdot s^{-1}$ to investigate its electrochemical reaction behavior and reversibility. The three curves in the figure correspond to the 1st (red), 2nd (blue), and 3rd (green) CV scanning cycles.

Two cathodic peaks can be clearly observed at 0.45 V and 0.9 V, indicating the intercalation of Zn^{2+} into the electrode material within this potential range. Meanwhile, the anodic peaks at 0.8 V and 1.1 V correspond to the Zn^{2+} deintercalation process. The presence of these redox peaks suggests that PANI-V_2O_5follows a typical Zn^{2+}intercalation/deintercalation mechanism, effectively facilitating charge storage and providing theoretical support for its excellent electrochemical performance.

Furthermore, the overlapping degree of the CV curves demonstrates that PANI-V_2O_5 exhibits good reversibility and cycling stability in the initial cycles. The three CV curves align closely, indicating a stable electrochemical reaction kinetics during Zn^{2+} intercalation/deintercalation. It is

Preprints.org (www.preprints.org) | NOT PEER-REVIEWED | Posted: 30 March 2025 doi:10.20944/preprints202503.2231.v1

worth noting that the first CV cycle differs slightly from the subsequent cycles, which can be attributed to the initial activation of active sites on the electrode material. As cycling progresses, the material structure stabilizes, resulting in more consistent redox behavior.

The incorporation of PANI plays a crucial role in optimizing electrochemical performance. On the one hand, PANI possesses good electrical conductivity, which enhances electron transport efficiency and accelerates Zn^{2+} intercalation/deintercalation kinetics. On the other hand, its mesoporous structure facilitates electrolyte penetration, providing a smoother pathway for Zn^{2+} migration. This synergistic effect not only improves the specific capacity of the material but also enhances its cycling stability.

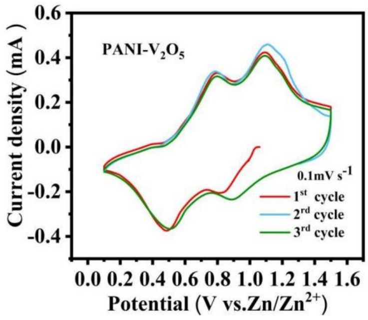

Figure 6. Cyclic voltammetry (CV) curves of PANI-V_2O_5 at a scan rate of 0.1 mV·s^{-1}.

3.2. Constant Current Charge-Discharge and Cycling Rate Performance Tests

Figure 7 shows the electrochemical performance of PANI-V_2O_5 and V_2O_5 under different testing conditions.

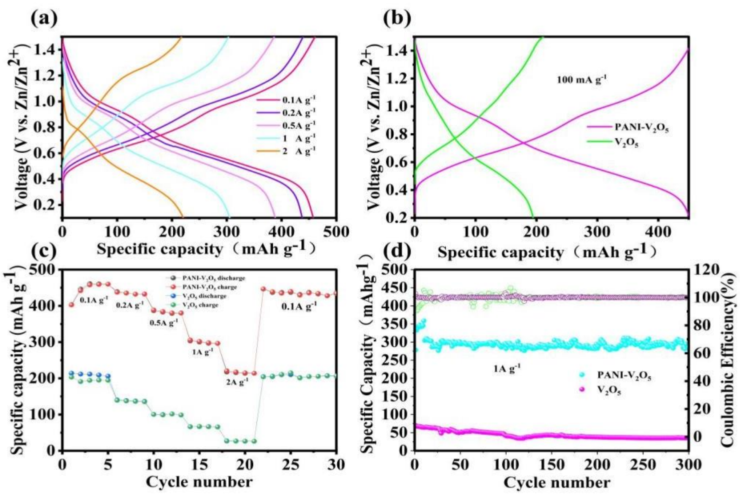

Figure 7. Comparison of electrochemical performance between PANI-V_2O_5 and V_2O_5. (**a**) First charge-discharge curves of PANI-V_2O_5 at different current densities; (**b**) Comparison of charge-discharge curves of PANI-V_2O_5 and V_2O_5 at 0.1 A g^{-1}; (**c**) Rate performance of the two materials at different current densities; (**d**) Cycling stability and coulombic efficiency trends of PANI-V_2O_5 and V_2O_5 at 1 A g^{-1} current density.

Figure 7a displays the charge-discharge curves of PANI-V_2O_5 at different current densities (0.1, 0.2, 0.5, 1, 2 A·g^{-1}). It can be seen that at a lower current density (0.1 A·g^{-1}), PANI-V_2O_5 exhibits a high specific capacity. As the current density increases, the capacity slightly decreases but still maintains good reversibility, indicating that the material has good rate capability.

Figure 7b compares the charge-discharge curves of PANI-$V_2O_5$and the original V_2O_5 at 100 mA·g^{-1}. From the figure, it is clear that PANI-V_2O_5 has a discharge capacity of 450 mAh·g^{-1}, which is

Preprints.org (www.preprints.org) | NOT PEER-REVIEWED | Posted: 30 March 2025 doi:10.20944/preprints202503.2231.v1

much higher than the original V_2O_5 (194 $mAh{\cdot}g^{-1}$). This significant improvement is mainly attributed to the introduction of PANI, which effectively enhances the Zn^{2+} storage capacity of the material.

Figure 7c further shows the rate performance of the materials at different current densities. It can be seen that the specific capacities of PANI-V_2O_5 at 0.1, 0.2, 0.5, 1, and 2 $A{\cdot}g^{-1}$ are 450, 435, 384, 305, and 220 $mAh{\cdot}g^{-1}$, respectively, demonstrating excellent Zn^{2+}storage capacity. Notably, when the current density is restored to 0.1 $A{\cdot}g^{-1}$, the specific capacity can recover to 450 $mAh{\cdot}g^{-1}$, indicating that the material maintains good reversibility and stability during high-rate charge-discharge processes. In contrast, V_2O_5shows poorer rate performance, with a faster decline in capacity.

Figure 7d shows the long-term cycling performance of PANI-V_2O_5 and V_2O_5 at a current density of 1 $A{\cdot}g^{-1}$. It can be seen that the capacity of V_2O_5 sharply decreases after 300 cycles, retaining only about 51.1% of its initial capacity, which is related to the instability of its structure and the dissolution of the material during the Zn^{2+}insertion/extraction process. In contrast, PANI-V_2O_5 retains 96.7% of its capacity, with an average cycle decay rate of only 0.0233%, demonstrating excellent cycling stability. Moreover, the coulombic efficiency remains close to 100%, indicating that the material undergoes minimal side reactions and has good electrochemical reversibility during long-term cycling.

3.3. Electrochemical Kinetics Analysis

To better understand the electrochemical reaction behavior of the PANI-V_2O_5 electrode, CV curves at different scan rates (0.1~1.0 $mV{\cdot}s^{-1}$) are tested. Figure 8 displays the electrochemical kinetics characteristics of PANI-V_2O_5, primarily analyzing its redox behavior, pseudocapacitive contribution, and trends with varying scan rates.

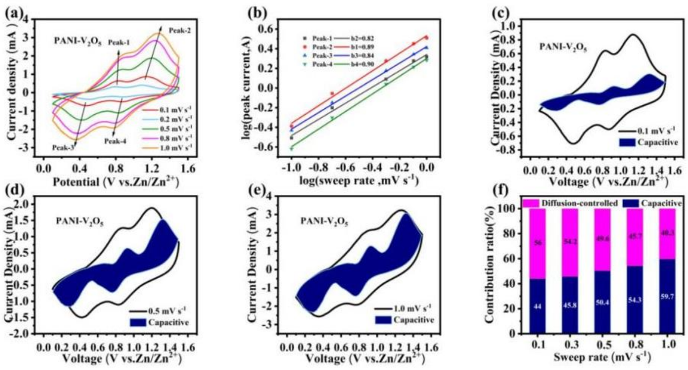

Figure 8. Electrochemical kinetic characteristics of the PANI-V_2O_5 electrode. (**a**) Cyclic voltammetry (CV) curves of PANI-V_2O_5 at different scan rates; (**b**) Log(i) vs. Log(v) relationship curve corresponding to the oxidation and reduction peaks in the CV; (**c**–**e**) Pseudocapacitive contribution separation curves at scan rates of 0.1, 0.5, and 1.0 $mV\ s^{-1}$; (**f**) Comparison of capacitive storage and diffusion-controlled contributions at different scan rates.

Figure 8a shows the cyclic voltammetry (CV) curves of the PANI-V_2O_5 electrode at different scan rates (0.1 ~ 1.0 $mV{\cdot}s^{-1}$). It can be observed that as the scan rate increases, the oxidation and reduction peaks shift to different potentials, with the oxidation peak moving to a higher potential and the reduction peak to a lower potential. This is mainly attributed to the enhanced polarization effect at higher scan rates, which is due to the limitations in the electrode's kinetic process. However, the CV curves maintain similar shapes, indicating good electrochemical reversibility and stability of PANI-V_2O_5.

Moreover, the relationship between current (i) and scan rate (v) can be used to determine the kinetic mechanism of the electrode reaction. Generally, the peak current (i) and scan rate (v) follow a power-law relationship:

$$i = av^b \tag{1}$$

Preprints.org (www.preprints.org) | NOT PEER-REVIEWED | Posted: 30 March 2025 doi:10.20944/preprints202503.2231.v1

where *a* and *b* are constants, and the value of *b* ranges from 0.5 to 1. When *b* is close to 0.5, the process is mainly diffusion-controlled, indicating that ions diffuse into the electrode material's lattice. When *b* is close to 1, the charge storage is mainly dominated by surface pseudocapacitive behavior. Based on this relationship, the pseudocapacitive contribution of the PANI-V_2O_5 electrode can be further explored to reveal its excellent electrochemical performance.

Figure 8b shows the linear relationship between the logarithmic peak current (log(*i*)) and the logarithmic scan rate (log(*v*)) of the redox peaks. By fitting the slopes of the different oxidation and reduction peaks, the values of *b* are obtained to determine the dominant charge storage mechanism. The calculated *b* values for the four oxidation and reduction peaks are 0.82, 0.89, 0.84, and 0.90, all close to 1, indicating that the charge storage process in the PANI-V_2O_5 electrode is primarily dominated by surface-induced pseudocapacitive behavior, rather than a purely diffusion-controlled process. This pseudocapacitive effect helps improve the electrode's rate performance and fast charge-discharge capability.

To further quantitatively analyze the contribution of pseudocapacitance to the total capacity, the following mathematical relationship can be used [41]:

$$i = k_1 v + k_2 v^{0.5} \tag{2}$$

where k_1 represents the pseudocapacitive contribution and k_2 represents the diffusion-controlled contribution. Eq.(2) shows that the proportion of pseudocapacitance and diffusion control varies with scan rate.

Figure 8c–e further analyze the pseudocapacitive contribution of the PANI-V_2O_5 electrode at different scan rates (0.1, 0.5, 1.0 $mV{\cdot}s^{-1}$). The shaded area represents the current density contributed by the pseudocapacitive process. Based on the calculations from Eq.(2), at a scan rate of 0.1 $mV{\cdot}s^{-1}$, the pseudocapacitive contribution is approximately 44%. As the scan rate increases from 0.1 $mV{\cdot}s^{-1}$ to 1.0 $mV{\cdot}s^{-1}$, the pseudocapacitive contribution gradually increases, reaching up to 59.7%. This trend indicates that at high scan rates, the pseudocapacitive contribution becomes more dominant, giving PANI-V_2O_5 excellent rate performance and fast kinetic response. This characteristic is important for improving the charging and discharging efficiency and power density of batteries in practical applications.

Figure 8f visually displays the contribution ratios of pseudocapacitive and diffusion-controlled processes to the total capacity at different scan rates. At a low scan rate (0.1 $mV{\cdot}s^{-1}$), the diffusion-controlled process contributes relatively more (approximately 55.6%), indicating that at low scan rates, Zn^{2+} primarily inserts/extracts into/from the electrode material via a diffusion mechanism. As the scan rate increases to 1.0 $mV{\cdot}s^{-1}$, the pseudocapacitive contribution ratio increases from 44.3% to 59.7%, showing that at high scan rates, the pseudocapacitive effect dominates, providing PANI-V_2O_5 with excellent rate performance.

4. Conclusions

This paper addresses the key issues of poor cycling stability and insufficient rate performance in zinc-ion batteries (ZIBs) by innovatively proposing an in-situ intercalation polyaniline (PANI) molecular modification strategy. Using a synchronous oxidative polymerization method, PANI-V_2O_5 organic-inorganic hybrid materials with a flower-cluster-like microstructure are successfully synthesized using vanadates and aniline as precursors, without the involvement of inert cations.

Experimental results show that this material exhibits significant advantages in electrochemical performance. At a current density of 0.1 $A{\cdot}g^{-1}$, the PANI-V_2O_5 hybrid material achieves a specific capacity of up to 450 $mAh{\cdot}g^{-1}$, far exceeding that of conventional V_2O_5 materials, demonstrating its huge potential for zinc-ion storage applications. Moreover, after 300 cycles at a high current density of 1 A g^{-1}, the capacity retention of the material remains as high as 96.7%, fully proving its excellent cycling stability.

The introduction of PANI effectively expands the interlayer spacing of V_2O_5, promoting the rapid reversible intercalation/de-intercalation of Zn^{2+}, while enhancing the material's electronic

Preprints.org (www.preprints.org) | NOT PEER-REVIEWED | Posted: 30 March 2025 doi:10.20944/preprints202503.2231.v1

conductivity, thereby optimizing the rate performance and long-term stability of the zinc-ion battery. Compared to traditional V_2O_5 electrode materials, the in-situ intercalation PANI molecular modification strategy proposed in this study not only significantly improves the electrochemical performance of the electrode material but also provides a new approach for designing novel high-performance cathode materials for zinc-ion batteries.

Author Contributions: Writing—original draft preparation, S.L.; writing—review and editing, T.Z., M.L., Y.L., Y.C., and X.L. ; validation, Y.L. and Q.Z. All authors have read and agreed to the published version of the manuscript.

Funding: This research was funded by the Natural Science Foundation of Hunan Province, China (Grant NO. 2023JJ50499, NO. 2023JJ50493) and was supported by the Scientific Research Fund of Hunan Provincial Education Department (NO. 23B0807).

Data Availability Statement: All the datasets used in this manuscript are publicly available datasets already in the public domain.

Conflicts of Interest: The authors declare no conflicts of interest.

References

1. Hu A, Chen W, Li F, et al. Nonflammable Polyfluorides-Anchored Quasi-Solid Electrolytes for Ultra-safe Anode-free Lithium Pouch Cells without Thermal Runaway [J]. Advanced Materials, 2023, 35(51): 2304762.
2. Yang B, Pan Y, Li T, et al. High-safety lithium Metal Pouch Cells for Extreme Abuse Conditions by Implementing Flame-Retardant Perfluorinated Gel Polymer Electrolytes [J]. Energy Storage Materials, 2024, 65: 103124.
3. Zhao C, Yan Z, Zhou B, et al. Identifying the Role of Lewis-Base Sites for The Chemistry in Lithium-Oxygen Batteries [J]. Angewandte Chemie International Edition, 2023, 62(32): 202302746.
4. Fang C, Li J, Zhang M, et al. Quantifying Inactive Lithium in Lithium Metal Batteries [J]. Nature, 2019, 572(7770): 511-515.
5. Wang P-F, Sui B-B, Sha L, et al. Nitrogen-rich Graphite Flake from Hemp as Anode Material for High Performance Lithium-Ion Batteries [J]. Chemistry – An Asian Journal, 2023, 18(13): 202300279.
6. Wang P, Gong Z, Wang D, et al. Facile Fabrication of F-doped Biomass Carbon as High-Performance Anode Material for Potassium-ion Batteries [J]. Electrochimica Acta, 2021, 389: 138799.
7. Quilty C D, Wu D, Li W, et al. Electron and Ion Transport in Lithium and Lithium-Ion Battery Negative and Positive Composite Electrodes [J]. Chemical Reviews, 2023, 123(4): 1327-1363.
8. Zhu Y, Ge M, Ma F, et al. Multifunctional Electrolyte Additives for Better Metal Batteries [J]. Advanced Functional Materials, 2024, 34(5): 2301964.
9. Yi X, Feng Y, Rao A M, et al. Quasi-Solid Aqueous Electrolytes for Low-Cost Sustainable Alkali-metal Batteries [J]. Advanced Materials, 2023, 35(29): 2302280.
10. Feng Y, Rao A M, Zhou J, et al. Selective Potassium Deposition Enables Dendrite-resistant Anodes for Ultrastable Potassium-Metal Batteries [J]. Advanced Materials, 2023, 35(30): 2300886.
11. Wang T, Sun J, Hua Y, et al. Planar and Dendrite-Free Zinc Deposition Enabled by Exposed Crystal Plane Optimization of Zinc Anode [J]. Energy Storage Materials, 2022, 53: 273-304.
12. Chen X, Sun W, Wang Y. Covalent Organic Frameworks for Next-Generation Batteries [J]. ChemElectroChem, 2020, 7(19): 3905-3926.
13. Shuai H, Xu J, Huang K. Progress in Retrospect of Electrolytes for Secondary Magnesium Batteries [J]. Coordination Chemistry Reviews, 2020, 422: 213478.
14. Meng Z, Foix D, Brun N, et al. Alloys to Replace Mg Anodes in Efficient and Practical Mg-Ion/SulfurBatteries [J]. ACS Energy Letters, 2019, 4(9): 2040-2044.
15. Liu J, Dong D, Caro A L, et al. Aqueous Electrolytes Reinforced by Mg and Ca Ions for Highly Reversible Fe Metal Batteries [J]. ACS Central Science, 2022, 8(6): 729-740.
16. Li H, Firby C J, Elezzabi A Y. Rechargeable Aqueous Hybrid Zn2+/Al3+ Electrochromic Batteries [J]. Joule, 2019, 3(9): 2268-2278.

17. Yi Z, Chen G, Hou F, et al. Strategies for The Stabilization of Zn Metal Anodes for Zn-Ion Batteries [J]. Advanced Energy Materials, 2021, 11(1): 2003065.
18. Xiao Y, Ren J, Li M, et al. Charge-Tuning Mediated Rapid Kinetics of Zinc Ions in Aqueous Zn-Ion Battery [J]. Chemical Engineering Journal, 2023, 474: 145801.
19. Huang J, Li Y, Xie R, et al. Structural Engineering of Cathodes for Improved Zn-Ion Batteries [J]. Journal of Energy Chemistry, 2021, 58: 147-155.
20. Tian Y, An Y, Liu C, et al. Reversible Zinc-Based Anodes Enabled by Zincophilic Antimony Engineered Mxene for Stable and Dendrite-Free Aqueous Zinc Batteries [J]. Energy Storage Materials, 2021, 41: 343-353.
21. Fu X, Li G, Wang X, et al. The Etching Strategy of Zinc Anode to Enable high Performance Zinc-Ion Batteries [J]. Journal of Energy Chemistry, 2024, 88: 125-143.
22. Blanc L E, Kundu D, Nazar L F. Scientific Challenges for the Implementation of Zn-Ion Batteries [J]. Joule, 2020, 4(4): 771-799.
23. Li S, Wei X, Wu C, et al. Constructing Three-Dimensional Structured V2O5/Conductive Polymer Composite with Fast Ion/Electron Transfer Kinetics for Aqueous Zinc-Ion Battery [J]. ACS Applied Energy Materials, 2021, 4(4): 4208-4216.
24. Shao Y, Zeng J, Li J, et al. Sandwich Structure of 3D Porous Carbon and Water-Pillared V2O5 Nanosheets for Superior Zinc-Ion Storage Properties [J]. ChemElectroChem, 2021, 8(10): 1784-1791.
25. Yang Y, Tang Y, Liang S, et al. Transition metal Ion-Preintercalated V2O5 as High-performance Aqueous Zinc-Ion Battery Cathode with Broad Temperature Adaptability [J]. Nano Energy, 2019, 61: 617-625.
26. Yang M, Wang Z, Ben H, et al. Boosting the Zinc ion Storage Capacity and Cycling Stability of Interlayer-Expanded Vanadium Disulfide Through In-Situ Electrochemical Oxidation Strategy [J]. Journal of Colloid and Interface Science, 2022, 607: 68-75.
27. Javed M S, Lei H, Wang Z, et al. 2D V2O5 Nanosheets as a Binder-free High-Energy Cathode for Ultrafast Aqueous and Flexible Zn-Ion Batteries [J]. Nano Energy, 2020, 70: 104573.
28. Lu Y, Wen Y, Huang F, et al. Rational Design and Demonstration of a High-Performance Flexible Zn/V2O5 Battery with Thin-Film Electrodes and Para-Polybenzimidazole Electrolyte Membrane [J]. Energy Storage Materials, 2020, 27: 418-425.
29. Wan F, Zhang L, Dai X, et al. Aqueous Rechargeable Zinc/Sodium Vanadate Batteries with Enhanced Performance from Simultaneous Insertion of Dual Carriers [J]. Nature Communications, 2018, 9(1): 520-529
30. Lv T-T, Liu Y-Y, Wang H, et al. Crystal Water Enlarging the Interlayer Spacing of Ultrathin V2O5·4VO2·2.72H2O Nanobelts for High-Performance Aqueous Zinc-Ion Battery [J]. Chemical Engineering Journal, 2021, 411: 128533.
31. Zhou S, Wu X, Du H, et al. Dual Metal Ions and Water Molecular Pre-Intercalated δ-MnO2 Spherical Microflowers for Aqueous Zinc Ion Batteries [J]. Journal of Colloid and Interface Science, 2022, 623: 456-466.
32. Li R, Xing F, Li T, et al. Intercalated Polyaniline in V2O5 as a Unique Vanadium Oxide Bronze Cathode for Highly Stable Aqueous Zinc Ion Battery [J]. Energy Storage Materials, 2021, 38: 590-598.
33. Yin C, Pan C, Liao X, et al. Regulating the Interlayer Spacing of Vanadium Oxide by In Situ Polyaniline Intercalation Enables an Improved Aqueous Zinc-Ion Storage Performance [J]. ACS Applied Materials & Interfaces, 2021, 13(33): 39347-39354.
34. Du Y, Xu Y, Zhang Y, et al. Metal-Organic-Framework-Derived Cobalt-Vanadium Oxides with Tunable Compositions for High-Performance Aqueous Zinc-Ion Batteries [J]. Chemical Engineering , 2023, 457: 141162.
35. Yang B, Tamirat A G, Bin D, et al. Regulating Intercalation of Layered Compounds for Electrochemical Energy Storage and Electrocatalysis [J]. Advanced Functional Materials, 2021, 31(52): 2104543.
36. Liu N, Wu X, Fan L, et al. Intercalation Pseudocapacitive Zn2+ Storage with Hydrated Vanadium Dioxide toward Ultrahigh Rate Performance [J]. Advanced Materials, 2020, 32(42): 1908420.
37. Tang H, Peng Z, Wu L, et al. Vanadium-Based Cathode Materials for Rechargeable Multivalent Batteries: Challenges and Opportunities [J]. Electrochemical Energy Reviews, 2018, 1(2): 169-199.

 doi:10.20944/preprints202503.2231.v1

38. Wang F, Sun W, Shadike Z, et al. How Water Accelerates Bivalent Ion Diffusion at the Electrolyte/Electrode Interface [J]. Angewandte Chemie International Edition, 2018, 57(37): 11978-11981.
39. Li W, Han C, Gu Q, et al. Electron Delocalization and Dissolution-Restraint in Vanadium Oxide Superlattices to Boost Electrochemical Performance of Aqueous Zinc-Ion Batteries [J]. Advanced Energy Materials, 2020, 10(48): 2001852.
40. Kumankuma-Sarpong J, Guo W, Fu Y. Yttrium Vanadium Oxide–Poly (3, 4-ethylenedioxythiophene) Composite Cathode Material for Aqueous Zinc-Ion Batteries [J]. Small Methods, 2021, 5(9): 2100544.
41. Zhang K, Hu Z, Liu X, et al. FeSe2 Microspheres as a High-Performance Anode Material for Na-Ion Batteries [J]. Advanced Materials, 2015, 27(21): 3305-3309.